J Adv Ceram

Research Article

Low-temperature formation of eutectic structures by reactive flash sintering of Al_2O_3–Y_2O_3 composites

Shu Yao[1,2,3], Xiang Xu[1,2,3], Liying Chen[1,2], Dianguang Liu[3], Yongsheng Liu[4], Ke Ren[5], Yiguang Wang[5], Jinling Liu[1,2,✉]

Cite this article: Yao S, Xu X, Chen L, et al. *J Adv Ceram* 2026, **15**(4): 9221268. https://doi.org/10.26599/JAC.2026.9221268

ABSTRACT: Reactive flash sintering (RFS) has garnered significant interest because of the simultaneous synthesis/reaction and sintering of multicomponent ceramic materials. While electric fields demonstrably accelerate reaction kinetics during RFS, the reciprocal effect of reactions on flash sintering (FS) remains unknown. In this study, the role of the solid-state reaction in the onset of FS was investigated using Al_2O_3–Y_2O_3 and Al_2O_3–$Y_3Al_5O_{12}$ (YAG) as models. The results show that the onset temperature of FS of Al_2O_3–Y_2O_3 is 350 °C lower than that of Al_2O_3–YAG under a constant electric field of 1000 V/cm. This demonstrates that the solid-state reaction significantly reduces the onset temperature, likely by enhancing the electrical conductivity of the sample. Remarkably, Al_2O_3–YAG ceramic composites with fine eutectic structures were prepared by RFS-ed Al_2O_3–Y_2O_3 at a furnace temperature of 850 °C, which is far below the eutectic temperature. The resultant eutectic ceramics exhibited mechanical properties comparable to those of conventionally solidified counterparts. RFS is expected to be an energy-efficient and sustainable sintering technology to fabricate high-performance eutectic ceramics.

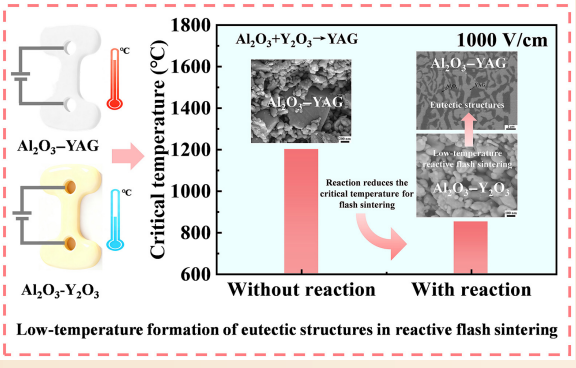

Low-temperature formation of eutectic structures in reactive flash sintering

KEYWORDS: reactive flash sintering (RFS); solid-state reaction; onset temperature; eutectic structures; mechanical properties

1 Introduction

Gaining high-density bulk multiphase ceramics via conventional sintering requires a long processing time at high temperature due to the low self-diffusion coefficient [1,2]. It not only imposes high demands on high-temperature equipment but also limits the large-scale industrialization of ceramic materials because of the high energy consumption over a long period of time. Consequently, developing novel sintering technology to fabricate multiphase ceramics with high performance under low temperatures and short sintering times has emerged as a critical objective in the field of ceramic manufacturing.

Flash sintering (FS) is a novel electric field-assisted sintering technique that enables ultrafast densification of ceramic materials at a furnace temperature far below the temperature required for conventional sintering [3]. For example, 3 mol% yttria-stabilized zirconia (3YSZ) ceramics can be densified in less than 5 s at a furnace temperature of 850 °C using a direct current (DC) electric field of 120 V/cm [3]. In contrast, conventional sintering of 3YSZ ceramics requires a temperature above 1450 °C for several hours. Consequently, the advantages of high efficiency and low energy consumption enable FS to be applied in various ceramic materials [4–10]. Based on the unique characteristic of low-temperature rapid mass transport of FS, researchers have further extended the application of FS, such as flash joining, rapid synthesis, plastic forming, and microstructure tailoring [11,12]. In 2016, Liu *et al.* [13] found that Y atoms can be incorporated into the lattice of monoclinic zirconia (m-ZrO_2) within 10 s to form tetragonal zirconia (t-ZrO_2) in the FS of Y_2O_3-doped pure m-ZrO_2. Shortly thereafter, Jha *et al.* [14] reported similar results in the alumina–titania (Al_2O_3–TiO_2) system. These findings demonstrate that the phase transformation in reactive multiphase ceramics can be accelerated by the electric field, implying an electric-field-driven cationic migration during FS. Building on this discovery, a derived technique known as reactive flash sintering/reaction-assisted flash sintering (RFS) was developed to synthesize ceramic materials with complex compositions [15,16].

The term RFS was first proposed in 2018 [15] and has attracted

[1] School of Mechanics and Aerospace Engineering, Southwest Jiaotong University, Chengdu 611756, China. [2] Advanced Structural Materials Mechanical Behavior and Service Safety Key Laboratory of Sichuan Province, Chengdu 611756, China. [3] School of Materials Science and Engineering, Southwest Jiaotong University, Chengdu 610031, China. [4] State Key Laboratory of Solidification Processing, Northwestern Polytechnical University, Xi'an 710072, China. [5] Institute of Advanced Structure Technology, Beijing Institute of Technology, Beijing 100081, China.

✉ Corresponding author. E-mail: liujinling@swjtu.edu.cn

Received: November 29, 2025; Revised: January 31, 2026; Accepted: February 19, 2026

significant interest owing to the realization of simultaneous chemical reactions and sintering of multiphase ceramics. Akin to FS, RFS possesses the advantages of low sintering temperature and short sintering time, without complex equipment. Most importantly, compared with conventional methods, the chemical reaction of precursors and sintering of ceramics are completed in one step during RFS [16–18]. These characteristics indicate that RFS is a more energy-efficient technology for the preparation of multiphase materials. To date, many RFS-ed materials have been reported, such as oxide ceramics [19–21], Li-ion conductors [22,23], and high-entropy ceramics [24,25]. RFS has certainly broadened the potential application of FS and has shown great advantages in screening novel materials, especially high-entropy ceramics. It is widely suggested that the solid-state reaction can be accelerated by applying an electric field [17]. Nevertheless, most RFS studies are dedicated to the preparation of materials and the optimization of flash parameters [26,27]. To the best of our knowledge, no prior studies have investigated the influence of solid-state reactions on the flash temperature of RFS, which is essential for a fundamental understanding of RFS.

In 2013, Zapata-Solvas *et al.* [6] added small amounts of Al_2O_3/Y_2O_3 into a SiC matrix and performed FS experiments. Their results indicate that the densification of SiC ceramics is promoted with the assistance of sintering aids during the FS process. Most importantly, they found that the onset temperature of FS of Al_2O_3/Y_2O_3-doped SiC is lower than that of pure SiC. The addition of Al_2O_3/Y_2O_3 enhanced the conductivity of the SiC matrix, reducing the onset temperature of FS. Recently, Zhang *et al.* [16] found that the reaction and densification of Al_2O_3–Y_2O_3 can be completed via RFS at 1350 °C for 30 s, whereas the preparation of dense Al_2O_3–YAG ceramic composites by hot pressing sintering requires 1600 °C for 2 h [28]. Their results further prove that the reaction is accelerated under the effect of a high electric field. However, the role of the solid-state reaction (Al_2O_3 + Y_2O_3 → YAG) on the onset of FS is still poorly investigated, which may be helpful in revealing the underlying mechanisms of RFS.

In this study, Al_2O_3–Y_2O_3 and Al_2O_3–YAG green bodies with a eutectic molar ratio were used to explore the effect of the solid-state reaction on the FS process. The results show that the onset temperature is greatly reduced due to the solid-state reaction. Furthermore, in our previous study [29], an Al_2O_3–YAG eutectic ceramic was obtained by flash sintering Al_2O_3–YAG composites at a furnace temperature of 1350 °C. Here, Al_2O_3–YAG eutectic ceramic can be directly prepared by RFS-ed Al_2O_3–Y_2O_3 at a low furnace temperature of 850 °C, which is far below the eutectic temperature (1820 °C).

2 Materials and methods

2.1 Preparation of green bodies

The raw materials used in this study were Y_2O_3 (99.99%, 30 nm), α-Al_2O_3 (99.99%, 170 nm), YAG (99.95%, 500 nm), and YAG (99.99%, 1–3 μm) powders. First, α-Al_2O_3 and Y_2O_3, in a eutectic molar ratio of 80.8 : 19.2, were uniformly mixed in deionized water for 50 h by using a powder mixer at 90 r/min. Then, the slurry was baked at 80 °C for 24 h using an oven. The resulting powder was ground and uniaxially pressed at 200 MPa to obtain dog-bone-shaped green bodies. The green bodies were then presintered from room temperature to 800 °C at a ramp rate of 2 °C/min and dwelled for 2 h. Finally, two holes, with a diameter of 1.60±0.01 mm, were drilled on both ends of the dog-bone green bodies to connect with Pt wires. The measured gauge section of the sample was 9.80 mm × 2.85 mm × 1.40 mm. In addition, pure Al_2O_3, Y_2O_3, and YAG green bodies were also prepared by pressing at 200 MPa.

For comparison, three types of Al_2O_3–YAG green bodies were prepared: (i) AY-1 was obtained from Al_2O_3–Y_2O_3 green bodies under calcination at 1350 °C for 10 min; (ii) AY-2 was obtained from α-Al_2O_3 and YAG (1–3 μm) with a eutectic molar ratio of 79.2 : 20.8; and (iii) AY-3 was obtained from α-Al_2O_3 and YAG (500 nm) with a eutectic molar ratio of 79.2 : 20.8. The preparation process of AY-2 and AY-3 was the same as that of the Al_2O_3–Y_2O_3 green bodies. The relative density of all green bodies was approximately 53%–56%, and the microstructures of the Al_2O_3–Y_2O_3, AY-1, AY-2, and AY-3 green bodies are presented in Fig. 1.

2.2 Flash-sintering experiments

The FS experiments were operated in a modified box furnace. The green bodies were placed in the center of the furnace via high-purity Pt wires and heated to a fixed temperature (T_f) at a rate of 10 °C/min. A constant electric field of 1000 V/cm via a DC power supply (APS DCP1200V-1A, Adaptive Power System, USA) was applied to the green bodies after maintaining for 10 min at T_f. Judging the occurrence of FS according to the change in current determined the onset temperature under a constant electric field of 1000 V/cm.

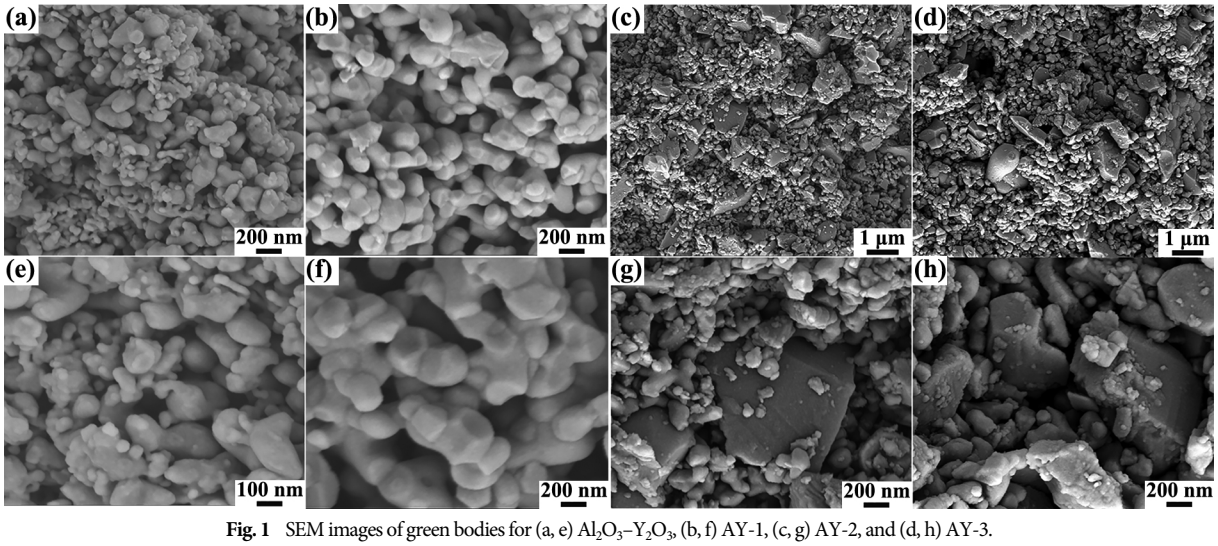

Fig. 1 SEM images of green bodies for (a, e) Al_2O_3–Y_2O_3, (b, f) AY-1, (c, g) AY-2, and (d, h) AY-3.

Furthermore, other FS experiments for pure Al_2O_3, Y_2O_3, YAG, and Al_2O_3–YAG were designed. A constant electric field of 1000 V/cm was applied to the green bodies at room temperature via a DC power supply, and the green bodies were heated at a rate of 10 °C/min until the occurrence of FS. The current density rapidly reached the preset value of 20 mA/mm^2, and then the power supply transitioned from voltage control to current control mode. The furnace temperature at which the FS occurred in these experiments was named the flash temperature.

2.3 Sample characterization

The relative density of the samples was measured by Archimedes' method with deionized water as the medium. The theoretical densities of Al_2O_3, Y_2O_3, and YAG are 3.99, 5.01, and 4.55 g/cm^3, respectively. The phase compositions of the samples were determined using an X-ray diffractometer (XRD; PANalytical Empyrean, Netherlands) with a Cu Kα radiation source (λ = 1.54 Å). The microstructure of the samples was observed using a field-emission scanning electron microscope (FESEM; Sigma 500, ZEISS, Germany). The element analysis was performed via an energy dispersive spectrometer (EDS; OXFORD X-Max 80, UK). The Vickers hardness and fracture toughness were measured using a Vickers hardness tester (200HV-5, Laizhou Huayin Test Instrument Co., Ltd., China) on the polished surface under an indentation load of 9.8 N for 15 s. At least 10 measurements were collected on each sample to obtain a reliable set of data.

3 Results and discussion

3.1 Reduction of onset temperature due to solid-state reaction

Figure 2 shows the XRD patterns for Al_2O_3–Y_2O_3 green bodies calcined at different temperatures. After calcining at 850 °C for 10 min, the Al_2O_3–Y_2O_3 green bodies are still composed of Al_2O_3 and Y_2O_3 without any additional phase. This indicates that the reaction of Al_2O_3 + Y_2O_3 → YAG has not yet begun at this temperature. Furthermore, the formation of intermediate phases $Y_4Al_2O_9$ (YAM) and $YAlO_3$ (YAP) with increasing temperature indicates that the reaction has initiated. Finally, the compositions of green bodies are transformed to Al_2O_3 and YAG under calcination at 1350 °C for 10 min. This indicates that the reaction has finished under these conditions.

Figure 3(a) depicts the plot of current density as a function of temperature for pure Al_2O_3 under a constant electric field of 1000 V/cm with a current limit of 20 mA/mm^2. There is a weak current after the furnace temperature rises to 1700 °C, but no conductivity surge finally occurs. This indicates that pure Al_2O_3 is difficult to flash due to the high electrical resistivity [30,31]. In fact, the flash temperature of FS of MgO-doped Al_2O_3 is also as high as 1260 °C under the same electric field (Table 1) [30].

Recent research shows that the flash temperature of FS of pure Y_2O_3 is approximately 985 °C under 1000 V/cm [7]. In this study, the flash temperature of FS of pure Y_2O_3 is 933 °C under the same electric field (Table 1). Figure 3(b) presents the plots of current density as a function of time for pure Y_2O_3 at different furnace temperatures under 1000 V/cm. When the furnace temperature is 850 °C, no current surge is observed. This indicates that this

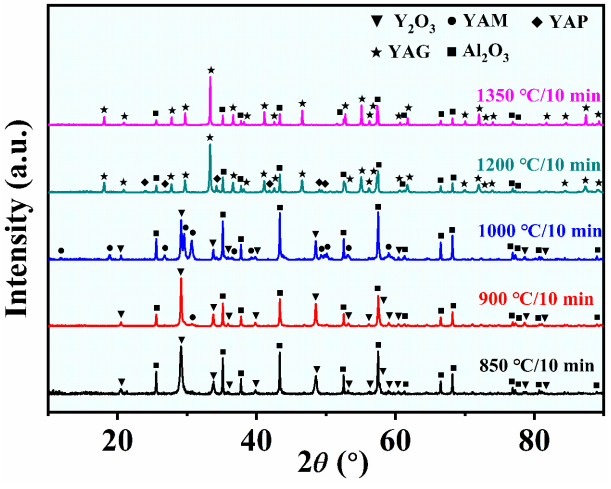

Fig. 2 (a) XRD patterns for Al_2O_3–Y_2O_3 green bodies calcined at different temperatures. Note that YAM and YAP denote $Y_4Al_2O_9$ and $YAlO_3$, respectively.

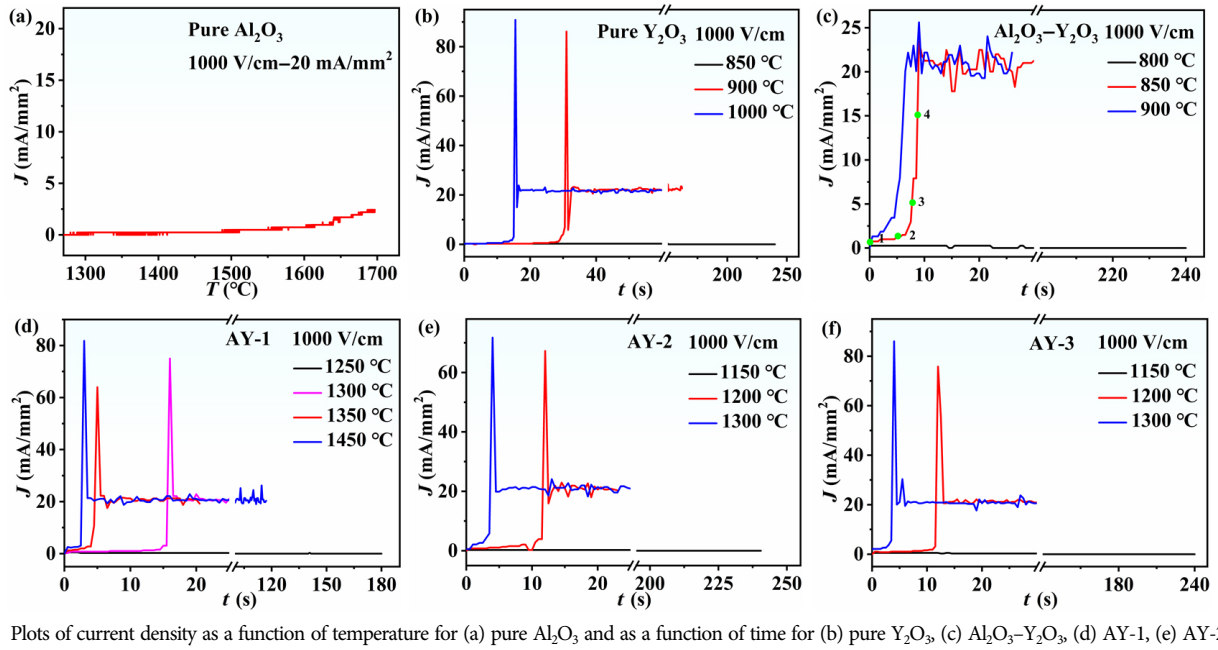

Fig. 3 Plots of current density as a function of temperature for (a) pure Al_2O_3 and as a function of time for (b) pure Y_2O_3, (c) Al_2O_3–Y_2O_3, (d) AY-1, (e) AY-2, and (f) AY-3.

temperature is not sufficient to ignite the FS of pure Y_2O_3. Furthermore, a typical characteristic of FS is presented in Fig. 3(b) when the furnace temperature is set to 900 °C [5]. After a period of incubation, the current rapidly reaches the peak value and then drops to the preset value. Hence, it can be concluded that the onset temperature of pure Y_2O_3 is 900 °C under 1000 V/cm. When the furnace temperature increases from 900 to 1000 °C, the incubation time is significantly shortened (Fig. 3(b)), which is similar to previous studies [5].

Figure 3(c) shows the plot of current density as a function of time for Al_2O_3–Y_2O_3 at fixed furnace temperatures. Pure Al_2O_3 or Y_2O_3 cannot be flash sintered at 850 °C under 1000 V/cm, but the Al_2O_3–Y_2O_3 mixtures can flash under these conditions. This result is obviously different from the FS of the Al_2O_3/YSZ composite; the onset temperature of the Al_2O_3/YSZ composite is between that of YSZ and pure Al_2O_3 under a constant electric field [32,33]. Furthermore, three types of Al_2O_3–YAG green bodies were chosen to perform FS experiments. Figures 3(d)–3(f) show the plots of current density as a function of time for AY-1, AY-2, and AY-3, respectively. The onset temperatures of AY-1, AY-2, and AY-3 are 1300, 1200, and 1200 °C, respectively, which are much higher than that of Al_2O_3–Y_2O_3 under the same electric field. It is supposed that the higher onset temperature of Al_2O_3–YAG than that of Al_2O_3–Y_2O_3 is due to the absence of a solid-state reaction [16].

Figure 4 presents the phase varying with time in the flash stage of Al_2O_3–Y_2O_3 in Fig. 3(c). Clearly, the solid-state reaction of Al_2O_3–Y_2O_3 was completed in the flash stage (point 4), which is similar to the result reported by Avila *et al.* [34]. Hence, it can be concluded that (i) the electric field accelerates the reaction rate [17], and (ii) the solid-state reaction may have some positive effects on the onset of FS. The reaction between Al_2O_3 and Y_2O_3, which is absent at 850 °C, is initiated and significantly accelerated under an electric field of 1000 V/cm. This electric-field-driven rapid reaction may enhance local electrical conductivity through the release of heat. On the other hand, the reaction process can generate a high concentration of point defects, further increasing the sample conductivity. The increase in the overall sample conductivity subsequently led to a reduction in the onset temperature of FS of Al_2O_3–Y_2O_3. Combined with these results, we propose that the reduction in the onset temperature of Al_2O_3–Y_2O_3 is related to the solid-state reaction between Al_2O_3 and Y_2O_3. That is, the reaction of Al_2O_3 + Y_2O_3 → YAG can promote the onset of FS.

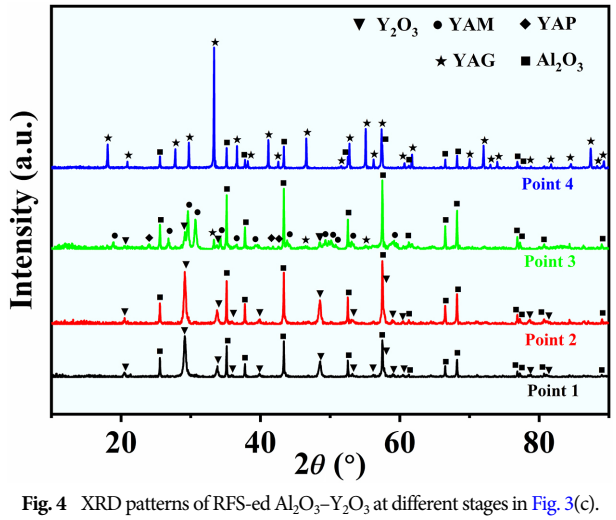

Fig. 4 XRD patterns of RFS-ed Al_2O_3–Y_2O_3 at different stages in Fig. 3(c).

3.2 Effect of interfaces on onset of flash sintering

Two key observations are evident from Table 1: (1) Pure Al_2O_3 or YAG is difficult to flash, whereas the Al_2O_3–YAG composites (AY-1, AY-2, and AY-3) can be flashed at lower temperatures, and (2) the onset temperature of AY-1 is 100 °C higher than AY-2 and AY-3 under the same electric field. A similar phenomenon was observed by Yang *et al.* [35] in Al_2O_3–$LaPO_4$ systems, which they attributed primarily to the heterointerfaces in the multiphase system. It is well established that electrical conductivity plays a decisive role in triggering the onset of FS [36]. Thus, the high resistivity of both Al_2O_3 and $LaPO_4$ makes them difficult to flash. However, when the two are mixed, the resistance of the grain boundaries between the phases may be smaller than the resistance of the crystal matrix. Under the combined effects of the electric field and elevated temperature, current preferentially flows through the grain boundaries, leading to localized Joule heating. This will further reduce the resistance and ultimately trigger FS [37].

Furthermore, the Al_2O_3–YAG green bodies used here were primarily prepared via two routes: high-temperature reaction (AY-1) and mechanical mixing (AY-2 and AY-3). Figure 1 presents the microstructure of the green bodies obtained by these two methods, along with the contact characteristics between the particles. The interfacial contact between Al_2O_3 and YAG differs significantly between these two types. For AY-1, Y_2O_3 particles dissolve into part of the Al_2O_3 particles under a high-temperature condition. The interfaces of Al_2O_3/YAG are formed through atom rearrangement at the atomic scale. Thus, the interfacial bonding of Al_2O_3/YAG is a chemical bonding. In contrast, AY-2 and AY-3, prepared by mechanical mixing, exhibit physical contact between Al_2O_3 and YAG particles. The Al_2O_3/YAG interface in AY-1 is formed through high-temperature diffusion, which is thermodynamically more stable and possesses a lower intrinsic point defect concentration. The Al_2O_3/YAG interfaces in AY-2 and AY-3 are in a higher energy state, which may facilitate the generation of structural defects under the effect of a high electric field. Consequently, AY-1 requires higher furnace temperatures to initiate FS, as shown in Table 1. Moreover, the particle size, powder dispersion, and neck growth also have significant effects on the FS behaviors [19,38,39]. Hence, the effect of the connectivity of particles on the onset of FS in multiphase ceramics needs further investigation.

3.3 Effect of temperature and electric field on solid-state reaction

Previous literature has confirmed that the diffusion of Y^{3+} can be

Table 1 Electric field and temperature required for FS of different ceramics

Material	Applied electric field (V/cm)	Flash temperature (°C)	Onset temperature (°C)
MgO-doped Al_2O_3 [30]	1000	1260	—
Y_2O_3 [7]	1000	985	—
Al_2O_3	1000	—	—
Y_2O_3	1000	933	900
YAG	1000	1507	—
Al_2O_3–Y_2O_3	1000	—	850
AY-1	1000	1478	1300
AY-2	1000	1422	1200
AY-3	1000	1442	1200

driven into Al_2O_3 to form metastable phases, such as YAM and YAP. As the temperature increases, the solid-phase reactions between Al_2O_3 and Y_2O_3 are given by Reactions (1)–(3) [40]:

$$2Y_2O_3 + Al_2O_3 = Y_4Al_2O_9\ (900 - 1000\,^{\circ}C) \quad (1)$$

$$Y_4Al_2O_9 + Al_2O_3 = 4YAlO_3\ (1100 - 1250\,^{\circ}C) \quad (2)$$

$$3YAlO_3 + Al_2O_3 = Y_3Al_5O_{12}\ (1400 - 1600\,^{\circ}C) \quad (3)$$

As shown in Fig. 2, the reaction of Al_2O_3 and Y_2O_3 begins to take place to form small amounts of YAM as the temperature increases from 850 to 900 °C. When the temperature further increases to 1000 °C, the continuous reaction between Al_2O_3 and Y_2O_3 produces a large number of YAM, leading to a drastic decrease in the Y_2O_3 content. When the temperature increases to 1200 °C, the YAM in the sample disappears. The sample is mainly composed of Al_2O_3, YAG, and a small amount of YAP. Until the temperature is increased to 1350 °C, YAP is thoroughly consumed through the reaction, and the Al_2O_3–Y_2O_3 is completely transformed into Al_2O_3 and YAG. The relationship between temperature and phase transformation is generally consistent with the results reported in the literature [40]. The synthesis of the YAG phase via conventional sintering requires maintaining temperatures above 1600 °C for a long time [41]. However, the phase transformation temperature of YAG in conventional sintering in the present study is much lower than 1600 °C. This is because the phase transformation is not only temperature dependent but also related to the particle size, mixing homogeneity of powders, and powder activity [41].

The XRD patterns of different positions for RFS-ed Al_2O_3–Y_2O_3 are shown in Fig. 5. Al_2O_3–Y_2O_3 is completely transformed into Al_2O_3 and YAG phases without any metastable phases. This indicates that the reaction is ended at a furnace temperature of 850 °C via RFS. The furnace temperature and reaction rate of RFS are much lower than those of conventional sintering [41]. As shown in Fig. 4, the solid-state reaction was completed during the flash stage. Throughout this process, the current passing through the sample gradually increased. The resulting Joule heating elevated the sample temperature above the furnace temperature. The atomic diffusion was promoted under high-temperature condition. However, the solid-state reaction was completed within seconds after applying a high electric field. The ultrafast reaction rate cannot be explained solely by Joule heating.

Furthermore, the interdiffusion of particles was accelerated due to the effect of the high electric field and temperature, and thereafter promoted the solid-state reaction. This process may be related to the formation of point defects induced by the electric field [17]. Akin to the FS of 3YSZ, the defect reaction (Reaction (4)) is presumed when a high electric field is applied to Y_2O_3 at high temperature [42]:

$$O_O^{\times} = \frac{1}{2}O_2 + V_O^{\cdot\cdot} + 2e' \quad (4)$$

During the incubation stage of FS, a high concentration of oxygen vacancies and electrons might be generated and incorporated into the sample. These point defects can act as charge carriers in samples. The electric field further promotes the migration of these charge carriers, thereby reducing the activation energy for atomic diffusion [43]. Therefore, it can be concluded that the ultrafast reaction rate results from the synergistic interaction between Joule heating and the electric field [17,21,23,24].

3.4 Formation of eutectic structures at low temperature

In our previous study [29], we successfully fabricated Al_2O_3–YAG eutectic ceramics by FS in less than 150 s at a furnace temperature of 1350 °C using Al_2O_3–YAG green bodies. Remarkably, similar eutectic structures were obtained in this study. It is noteworthy that the RFS-ed sample density attained only ~80%. This outcome can be attributed to two primary factors. First, the FS parameters used in this work were not optimized to achieve full densification. Second, density inhomogeneity is a common characteristic due to current localization in the FS process. While these factors led to a moderately low sample density, the microstructure in local regions of the samples remained dense. SEM images reveal that the samples mainly show two different microstructures: Al_2O_3–YAG polycrystalline and Al_2O_3–YAG eutectic structures, as shown in Fig. 6. Combined with Fig. 7, the black phase corresponds to Al_2O_3, and the gray phase corresponds to YAG. Both phases with irregular morphology are evenly distributed together, presenting a typical Al_2O_3–YAG ceramic composite (Fig. 6(a)). Notably, the furnace temperature for the preparation of the Al_2O_3–YAG ceramic composite via RFS of Al_2O_3–Y_2O_3 is 500 °C lower than that in our previous study [16]. This furnace temperature is also much lower than the temperature required for Al_2O_3–YAG ceramic composites prepared by conventional sintering [28]. The results indicate that the rapid mass transport of oxide ceramic composites can be achieved in a short time at a lower temperature via RFS.

Figure 6(b) exhibits a typical Al_2O_3–YAG eutectic structure with two alternating phase layers [44], the so-called Chinese script structure. Similar structures have been reported in the FS of other eutectic systems [35,45–47]. The morphology of the eutectic structure at different positions on the samples is shown in Fig. 8. The microstructure along the anode to the cathode is uneven. The eutectic near the anode and center mainly presents a Chinese script structure, while the eutectic near the cathode presents a typical colony structure. Additionally, the thickness of the eutectic layers is different at different positions. Compared with eutectic layers near the anode, there appears to be significant structure refinement for eutectic layers near the cathode and center. Liu *et al.* [48] found that the sample temperature of 8YSZ during FS presented an asymmetric distribution due to the electrochemical reaction. This suggests that the inhomogeneity of eutectic structures may be related to the uneven temperature distribution and internal reaction inside the sample during FS [49].

It is well known that the formation of eutectic structures usually

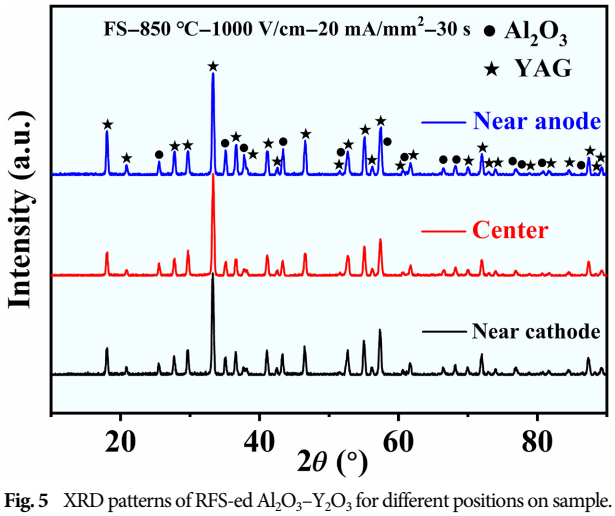

Fig. 5 XRD patterns of RFS-ed Al_2O_3–Y_2O_3 for different positions on sample.

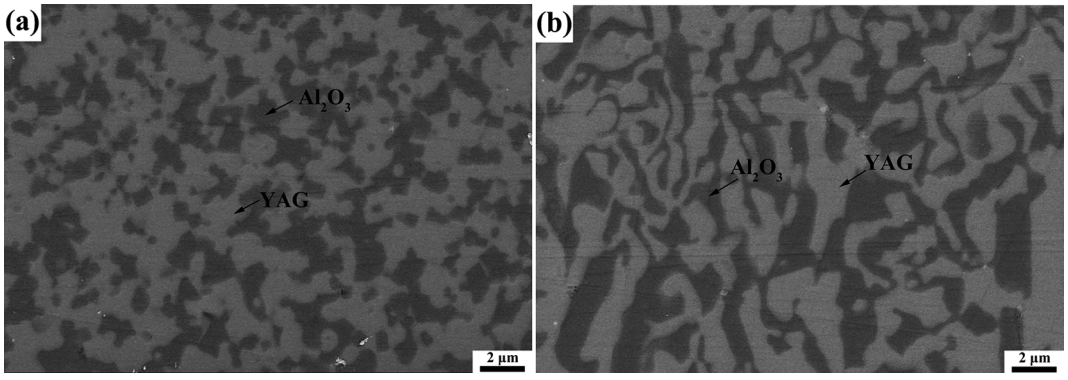

Fig. 6 SEM images of (a) Al_2O_3–YAG polycrystalline and (b) Al_2O_3–YAG eutectic ceramic prepared by RFS.

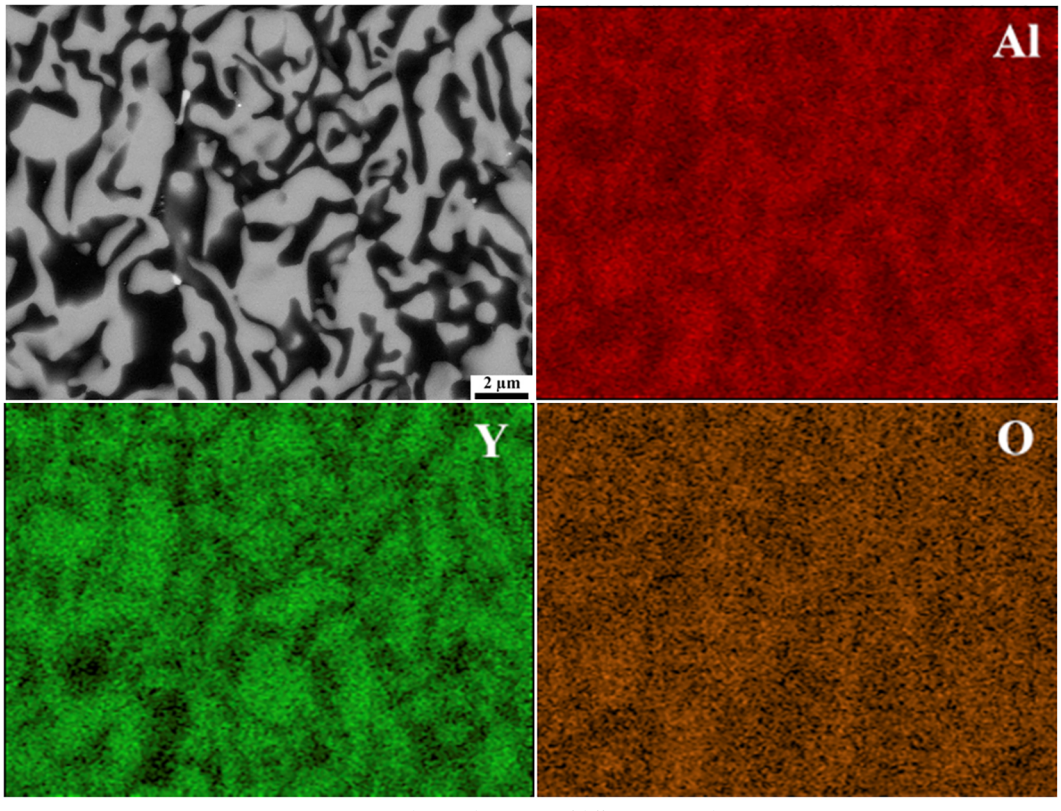

Fig. 7 EDS elemental mapping of different eutectic layers.

requires heating the green body above the eutectic temperature, and eutectic structures are formed by the solidification of the melt as it cools [50]. In fact, due to the Joule heating derived from the preset current, the sample temperature during FS is higher than the furnace temperature [51]. Furthermore, the current localization and the formation of hot spots are the main drawbacks in FS. These adverse effects will result in undesired sintering (melting, cracking, and inhomogeneous microstructure) of samples after FS treatment [8,11,39,52]. Hence, it is important to evaluate the sample temperature during RFS to determine the role of temperature in the formation of eutectic structures.

The sample temperature is mainly evaluated by two methods: observation by the thermal imaging camera and calculation by the black-body radiation model [51]. For example, Aoki *et al.* [46] observed the sample temperature evolution of Al_2O_3–$GdAlO_3$ composites by a thermal imaging camera during FS. They found that the highest sample temperature (~1750 °C) exceeds the eutectic temperature (1740 °C) in the stable stage of FS, resulting in the formation of Al_2O_3–$GdAlO_3$ eutectic structures. Similarly, Yang *et al.* [35] calculated the sample temperature of Al_2O_3–$LaPO_4$ composites in the stable stage of FS using the black-body radiation model. They also attributed the formation of Al_2O_3–$LaPO_4$ eutectic structures to the sample temperature exceeding the eutectic temperature. Based on these results, most researchers believe that the formation of eutectic structures is related to local melting due to current localization [35,45,46,53].

In the FS process, the sample temperature is determined by the furnace temperature and power dissipation. To weaken the influence of temperature on the formation of eutectic structures, a furnace temperature of 850 °C is chosen in this study, which is far lower than those studies relating to the formation of eutectic structures via FS [29,35,45,46]. In addition, to avoid the tremendous Joule heating induced by the current leading to melting or sample damage, we used a low current density (20 mA/mm^2) as the preset current limit. Most importantly, no significant current peak or only a relatively small current peak is generated in the flash stage of the low-current FS (Fig. 3(c)), which is favorable for the elimination of hot spots and melting. The

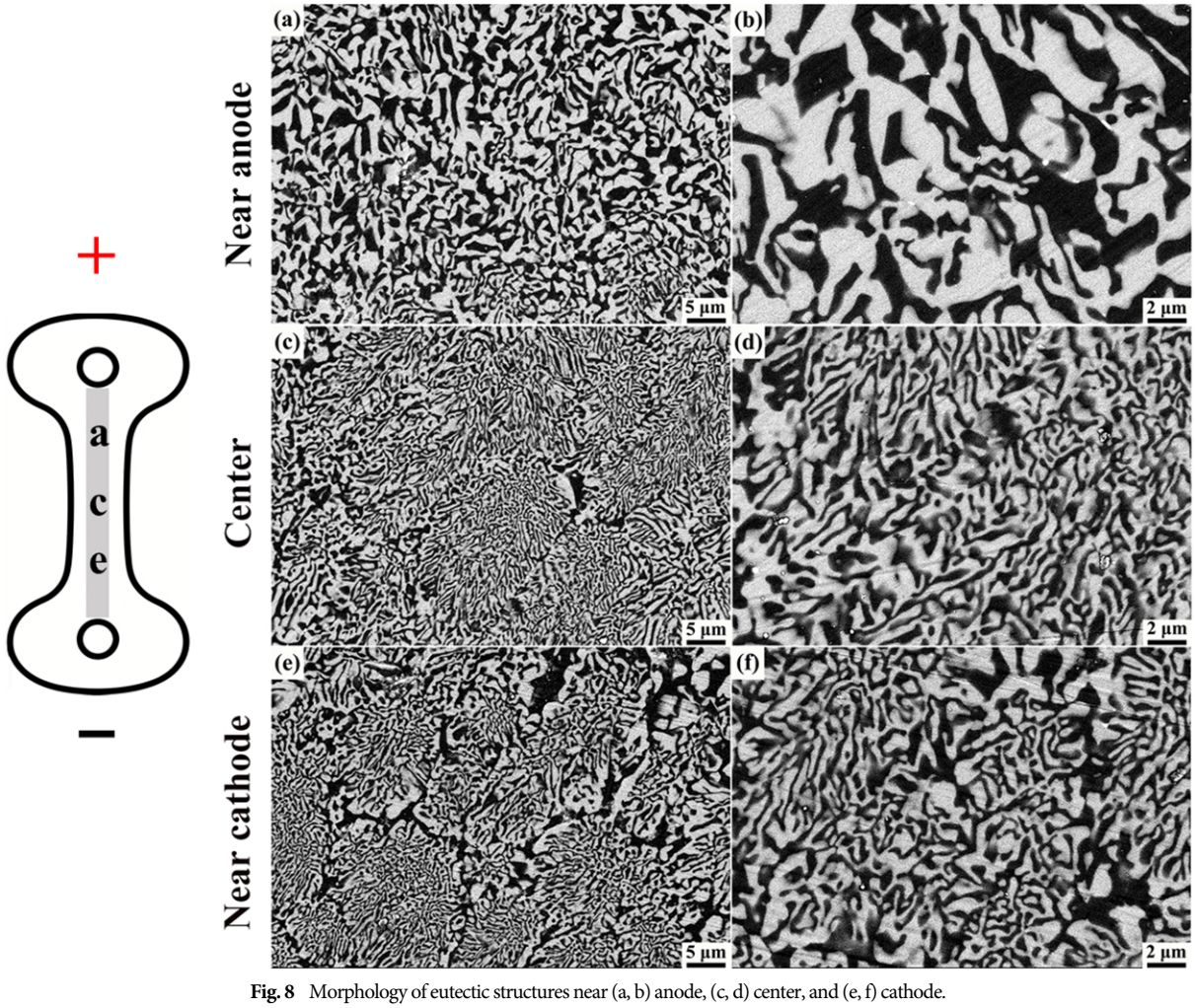

Fig. 8 Morphology of eutectic structures near (a, b) anode, (c, d) center, and (e, f) cathode.

sample temperature during FS was estimated by using the black-body radiation model, as given by Eq. (5) [51]:

$$T_e = \left(T_f^4 + \frac{W}{A\varepsilon\sigma}\right)^{1/4} \quad (5)$$

where T_e is the actual temperature of the samples (K); T_f is the furnace temperature (K); W is the power dissipation of the stable state (W); A is the surface area of the gauge section of the samples (m^2); σ represents the Stefan–Boltzmann constant (5.67×10^{-8} $W{\cdot}m^{-2}{\cdot}K^{-4}$); ε is the emissivity. Herein, the sample temperature of the RFS-ed sample was estimated to be 1138–1490 °C (ε is assumed to be 0.8–1) via the black-body radiation model, which is much lower than the eutectic temperature of the Al_2O_3–YAG eutectic system [54]. Large areas of eutectic structures can be produced in the presence of a relatively weak Joule heating effect, implying that local melting may not be able to reveal the mechanism for the formation of Al_2O_3–YAG eutectic structures. However, it is important to note that the black-body radiation model is idealized [51]. Its temperature estimation is influenced by current localization, often resulting in predicted values lower than the actual sample temperature. Additionally, the emissivity of Al_2O_3 is 0.47 [55], while a definitive value for YAG is not established. If a uniform emissivity of 0.47 is assumed for the Al_2O_3–YAG composite, the estimated temperature based on the black-body radiation model can exceed 2700 °C, which is far above the eutectic temperature. Consequently, temperatures calculated from this model should be treated as approximate references. Developing more accurate measurement techniques remains a critical challenge in the field of FS for preparing eutectic ceramics.

Furthermore, according to several studies [42,56–58], high-concentration defects, such as oxygen vacancies and dislocations, will be introduced into the samples, which may change the mechanisms of mass transport during the FS process. It is speculated that the formation of eutectic structures has been achieved under a solid-state process due to the effect of the electric field, and the role of Joule heating and the electric field in the formation of eutectic structures needs to be further scrutinized.

3.5 Mechanical properties of eutectic ceramics

Generally, oxide eutectic ceramics exhibit superior mechanical properties to composite ceramics with the same component due to their unique microstructure. For instance, the hardness and fracture toughness of FS-ed Al_2O_3–YAG composite ceramics are 13.4±0.2 GPa and 4.8±0.1 $MPa{\cdot}m^{1/2}$, respectively [16]. However, the hardness and fracture toughness of FS-ed Al_2O_3–YAG eutectic ceramics with the same mixing ratios reach 18.5±0.3 GPa and 4.3±0.2 $MPa{\cdot}m^{1/2}$ [29]. While eutectic ceramics exhibit comparable toughness to composite ceramics, their hardness is significantly greater. This suggests that eutectic ceramics have superior wear resistance compared with composite ceramics. Furthermore, Yang *et al.* [59] systematically investigated the Vickers and Knoop hardness of Al_2O_3–$LaPO_4$ composites with eutectic microstructures prepared by FS. Their results also indicate that the

eutectic structures exhibit higher hardness values than their polycrystalline counterparts.

The Vickers hardness and fracture toughness of eutectic ceramics are measured by the indentation technique. The average hardness of RFS-ed Al_2O_3–YAG eutectic ceramics was approximately 15.4±0.2 GPa, which was comparable to that of conventionally solidified counterparts [44,60–64], as shown in Table 2. The average toughness of the eutectic ceramics reached 3.1±0.2 MPa·m$^{1/2}$, which was significantly higher than that of the directionally solidified Al_2O_3–YAG eutectic ceramics (Table 2).

Driven by synergistic electric–thermal effects, the RFS process produces clean, strongly bonded Al_2O_3/YAG interfaces with minimal impurity segregation. These fine lamellar structures and the associated interfacial characteristics intrinsically enhance the mechanical properties of the eutectic ceramics. A typical indentation of Al_2O_3–YAG eutectic ceramics is shown in Fig. 9(a). The relatively high hardness is mainly ascribed to the refinement of the eutectic structure, where more interfaces act as dislocation obstacles to strengthen the eutectics [62]. Furthermore, when the crack forms and propagates through the fine and alternating two-phase structure, the crack can preferentially deflect along the well-bonded interphase boundaries. Figure 9(b) presents the interaction between the crack path and the eutectic phase interfaces. The superior toughness of RFS-ed eutectic ceramics is ascribed to toughening mechanisms such as crack deflection and crack bridging. The deflection and bridging can consume more fracture energy and prolong the crack propagation path, which improves the toughness of eutectic ceramics.

Notably, the hardness and toughness of RFS-ed Al_2O_3–YAG eutectic ceramics are lower than 17.5±2.0 GPa and 3.6±0.4 MPa·m$^{1/2}$ reported by Su *et al.* [62]. This is mainly because the interface spacing of the directionally solidified Al_2O_3–YAG eutectic is finer than that of the RFS-ed eutectic ceramics, endowing the eutectic ceramics with excellent mechanical properties. However, the sintering time of RFS is only 30 s. Liu *et al.* [29] found that eutectic structures continue to evolve during the stable stage of FS. Hence, the short sintering time may lead to weak bonding at the eutectic interfaces, thus negatively affecting the hardness of eutectic ceramics. In a word, RFS realized ultrafast and low-temperature preparation of Al_2O_3–YAG eutectic ceramics with mechanical properties comparable to directionally solidified eutectic ceramics. The above results indicate that RFS is expected to be a new technology for the preparation of eutectic ceramics with fine structures, and the process does not require complex devices and high energy consumption.

4 Conclusions

In summary, this study systematically investigated the influence of the solid-state reaction ($Al_2O_3 + Y_2O_3 \rightarrow$ YAG) on the onset of FS.

Table 2 Vickers hardness and fracture toughness of Al_2O_3–YAG eutectic ceramics prepared by RFS and other technologies

Ref.	Vickers hardness (GPa)	Fracture toughness (MPa·m$^{1/2}$)	Testing method
Present work	15.40±0.20	3.10±0.20	IM [a]
[44]	16.10	2.01	IM
[60]	15.00–16.00	2.00–2.40	IM
[61]	16.04±0.75	2.69±0.06	IM
[62]	17.50±2.00	3.60±0.40	IM
[63]	15.50±0.20	2.60±0.20	IM
[64]	13.50	3.10±0.30	IM

Note: [a] is an indentation method.

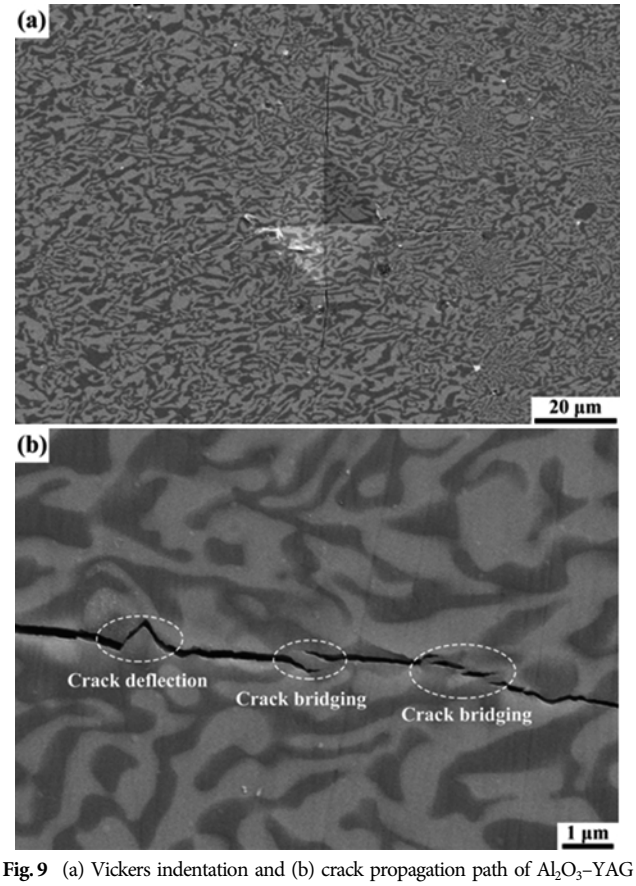

Fig. 9 (a) Vickers indentation and (b) crack propagation path of Al_2O_3–YAG eutectic ceramics.

Ultrafast reaction and densification of Al_2O_3–Y_2O_3 were achieved via RFS. The key findings are as follows:

(1) Compared with conventional sintering, RFS of Al_2O_3–Y_2O_3 enabled an ultrafast reaction and rapid mass transport at a low temperature of 850 °C. The results demonstrate that the solid-state reaction of Al_2O_3–Y_2O_3 is accelerated by applying an electric field. Most importantly, the reaction promotes the occurrence of FS, and the onset temperature is greatly reduced. Under a constant electric field, the onset temperature of FS of Al_2O_3–Y_2O_3 is 350 °C lower than that of Al_2O_3–YAG. The solid-state reaction lowers the onset temperature, likely because the electric-field-driven process enhances the sample conductivity.

(2) The characteristics of Al_2O_3/YAG interfaces formed via different processing routes influence the temperature required for FS. Chemically bonded interfaces synthesized through high-temperature reactions are thermodynamically more stable, whereas physically contacted interfaces created by mechanical mixing exist in a higher energy state. Consequently, under a constant electric field, the latter enables FS to occur at a lower temperature.

(3) Al_2O_3–YAG ceramic composites with large-area fine eutectic structures are prepared by RFS-ed Al_2O_3–Y_2O_3 at a furnace temperature far below the eutectic temperature in a short time. These results suggest that RFS is a more energy-efficient sintering technology and opens a new avenue to fabricate high-performance eutectic ceramics.

Acknowledgements

This work was financially supported by the National Natural Science Foundation of China (No. 52272074), the Department

of Science and Technology of Sichuan Province (No. 2021JDJQ0019), the State Key Laboratory of Solidification Processing in Northwestern Polytechnical University (NWPU) (No. SKLSP202104), and the Fundamental Research Funds for the Central Universities (Nos. 2682024GF011 and 2682024GF016).

Availability of data and materials

The data that support the findings of this study are available from the corresponding author upon reasonable request.

Competing interests

The authors have no competing interests to declare that are relevant to the content of this article. The author Jinling Liu is the Editorial Committee member of this journal.

References

[1] Rabinovich EM. Preparation of glass by sintering. *J Mater Sci* 1985, **20**: 4259–4297.

[2] Bordia RK, Kang SL, Olevsky EA. Current understanding and future research directions at the onset of the next century of sintering science and technology. *J Am Ceram Soc* 2017, **100**: 2314–2352.

[3] Cologna M, Rashkova B, Raj R. Flash sintering of nanograin zirconia in < 5 s at 850 °C. *J Am Ceram Soc* 2010, **93**: 3556–3559.

[4] Cologna M, Prette ALG, Raj R. Flash-sintering of cubic yttria-stabilized zirconia at 750 °C for possible use in SOFC manufacturing. *J Am Ceram Soc* 2011, **94**: 316–319.

[5] Francis JSC, Raj R. Influence of the field and the current limit on flash sintering at isothermal furnace temperatures. *J Am Ceram Soc* 2013, **96**: 2754–2758.

[6] Zapata-Solvas E, Bonilla S, Wilshaw PR, *et al.* Preliminary investigation of flash sintering of SiC. *J Eur Ceram Soc* 2013, **33**: 2811–2816.

[7] Yoshida H, Sakka Y, Yamamoto T, *et al.* Densification behaviour and microstructural development in undoped yttria prepared by flash-sintering. *J Eur Ceram Soc* 2014, **34**: 991–1000.

[8] Trombin F, Raj R. Developing processing maps for implementing flash sintering into manufacture of whiteware ceramics. *Am Ceram Soc Bull* 2014, **93**: 32–35.

[9] Li YJ, Chi QG, Yan ZY, *et al.* Flash sintering of high-purity alumina at room temperature. *J Adv Ceram* 2023, **12**: 2382–2388.

[10] Silva ECF, Silva RNR, Caraschi LC, *et al.* A comprehensive study on flash sintering of anatase and rutile polymorphs-containing titania nanopowder: Phase and microstructure development. *J Adv Ceram* 2025, **14**: 9221062.

[11] Biesuz M, Sglavo VM. Flash sintering of ceramics. *J Eur Ceram Soc* 2019, **39**: 115–143.

[12] Liu JL, Liu DG, Ren K, *et al.* Research progress on the flash sintering mechanism of oxide ceramics and its application. *J Inorg Mater* 2022, **37**: 473–480.

[13] Liu DG, Gao Y, Liu JL, *et al.* Effect of holding time on the microstructure and properties of flash-sintered Y_2O_3-doped ZrO_2. *Ceram Int* 2016, **42**: 17442–17446.

[14] Jha SK, Lebrun JM, Raj R. Phase transformation in the alumina–titania system during flash sintering experiments. *J Eur Ceram Soc* 2016, **36**: 733–739.

[15] Gil-González E, Perejón A, Sánchez-Jiménez PE, *et al.* Phase-pure $BiFeO_3$ produced by reaction flash-sintering of Bi_2O_3 and Fe_2O_3. *J Mater Chem A* 2018, **6**: 5356–5366.

[16] Zhang H, Wang YG, Liu JL, *et al.* Reaction assisted flash sintering of Al_2O_3–YAG ceramic composites with eutectic composition. *Ceram Int* 2019, **45**: 13551–13555.

[17] Yoon B, Avila V, Lavagnini IR, *et al.* Reactive flash sintering of ceramics: A review. *Adv Eng Mater* 2023, **25**: 2200731.

[18] Jesus LM, Silva RS, M'Peko JC. Ultrafast synthesis and sintering of materials in a single running experiment approach by using electric fields. *J Adv Ceram* 2019, **8**: 265–277.

[19] Yoon B, Avila V, Kathiria R, *et al.* Effects of powder dispersion on reactive flash sintering of 8 mol% yttria-stabilized zirconia and $MgAl_2O_4$ composites. *Scripta Mater* 2020, **189**: 117–121.

[20] Yoon B, Yadav D, Ghose S, *et al.* Reactive flash sintering: MgO and α-Al_2O_3 transform and sinter into single-phase polycrystals of $MgAl_2O_4$. *J Am Ceram Soc* 2019, **102**: 2294–2303.

[21] Zhu Y, Ma BS, Wang KW, *et al.* Electric field-assisted solid-state reaction of $BaCO_3$–TiO_2 system. *J Am Ceram Soc* 2021, **104**: 6572–6578.

[22] Shi PR, Qu GX, Cai SK, *et al.* An ultrafast synthesis method of $LiNi_{1/3}Co_{1/3}Mn_{1/3}O_2$ cathodes by flash/field-assisted sintering. *J Am Ceram Soc* 2018, **101**: 4076–4083.

[23] Zuo Q, Liu W, Chen GC, *et al.* The synthetic mechanism of $LiCoO_2$ from CoO and Li_2CO_3 under electric field. *J Adv Ceram* 2025, **14**: 9221105.

[24] Liu DG, Peng XY, Liu JL, *et al.* Ultrafast synthesis of entropy-stabilized oxide at room temperature. *J Eur Ceram Soc* 2020, **40**: 2504–2508.

[25] Mao HR, Guo RF, Cao Y, *et al.* Ultrafast densification of high-entropy oxide $(La_{0.2}Nd_{0.2}Sm_{0.2}Eu_{0.2}Gd_{0.2})_2Zr_2O_7$ by reactive flash sintering. *J Eur Ceram Soc* 2021, **41**: 2855–2860.

[26] Ingraci Neto RR, Kardoulaki E, Valdez JA. The influence of the processing parameters on the reactive flash sintering of ZrO_2–CeO_2. *J Am Ceram Soc* 2022, **105**: 3937–3948.

[27] An G, Fu MY, Jiao ZH, *et al.* Rapid preparation of $Bi_{0.5}Na_{0.5}TiO_3$ ceramics by reactive flash sintering of Bi_2O_3–$NaCO_3$–TiO_2 mixed powders. *J Eur Ceram Soc* 2022, **42**: 1407–1413.

[28] Yao B, Su HJ, Zhang J, *et al.* Sintering densification and microstructure formation of bulk Al_2O_3/YAG eutectic ceramics by hot pressing based on fine eutectic structure. *Mater Design* 2016, **92**: 213–222.

[29] Liu JL, Xu X, Liu DG, *et al.* Ultrafast formation of Al_2O_3–$Y_3Al_5O_{12}$ eutectic ceramic by flash sintering. *J Am Ceram Soc* 2020, **103**: 4051–4056.

[30] Cologna M, Francis JSC, Raj R. Field assisted and flash sintering of alumina and its relationship to conductivity and MgO-doping. *J Eur Ceram Soc* 2011, **31**: 2827–2837.

[31] Biesuz M, Luchi P, Quaranta A, *et al.* Theoretical and phenomenological analogies between flash sintering and dielectric breakdown in α-alumina. *J Appl Phys* 2016, **120**: 145107.

[32] Naik KS, Sglavo VM, Raj R. Field assisted sintering of ceramic constituted by alumina and yttria stabilized zirconia. *J Eur Ceram Soc* 2014, **34**: 2435–2442.

[33] Yao S, Chen LY, Liu DG, *et al.* The onset mechanism of flash sintering in Al_2O_3–8YSZ composites. *J Adv Ceram* 2025, **14**: 9221166.

[34] Avila V, Yoon B, Ingraci Neto RR, *et al.* Reactive flash sintering of the complex oxide $Li_{0.5}La_{0.5}TiO_3$ starting from an amorphous precursor powder. *Scripta Mater* 2020, **176**: 78–82.

[35] Yang YJ, Mumm DR, Mecartney ML. Flash sintering produces eutectic microstructures in Al_2O_3–$LaPO_4$ versus conventional microstructures in 8YSZ–$LaPO_4$. *J Am Ceram Soc* 2021, **104**: 3895–3909.

[36] Raj R. Analysis of the power density at the onset of flash sintering. *J Am Ceram Soc* 2016, **99**: 3226–3232.

[37] Zhou SY, Shen C, Estrella D, *et al.* Phase-boundary assisted flash sintering of Al_2O_3–TiO_2 nanocomposites. *Acta Mater* 2026, **302**: 121612.

[38] Francis JSC, Cologna M, Raj R. Particle size effects in flash sintering. *J Eur Ceram Soc* 2012, **32**: 3129–3136.

[39] Su XH, Zeng H, Tian YL, *et al.* Influence of pre-sintering on the reactive flash sintering of high-entropy rare earth zirconate ceramics. *J Eur Ceram Soc* 2026, **46**: 117901.

[40] Gusshkova VB, Krzhizhanovskaya VA, Egorova ON. Interactions of yttrium and aluminum oxide. *J Inorg Mater* 1983, **19**: 80–84.

[41] Wen L, Sun XD, Xiu ZM, *et al.* Synthesis of nanocrystalline yttria

powder and fabrication of transparent YAG ceramics. *J Eur Ceram Soc* 2004, **24**: 2681–2688.
[42] Yoshida H, Morita K, Kim BN, *et al.* Reduction in sintering temperature for flash-sintering of yttria by nickel cation-doping. *Acta Mater* 2016, **106**: 344–352.
[43] Liu DG, Li X, Liu FZ, *et al.* Effect of the current density on the densification of 3 mol% yttria-stabilized zirconia in flash sintering. *J Alloy Compd* 2020, **825**: 154061.
[44] Larrea A, Orera VM, Merino RI, *et al.* Microstructure and mechanical properties of Al_2O_3–YSZ and Al_2O_3–YAG directionally solidified eutectic plates. *J Eur Ceram Soc* 2005, **25**: 1419–1429.
[45] Sun F, Ji PC, Tan L, *et al.* Formation of eutectic microstructure in Al_2O_3–$GdAlO_3$–ZrO_2 ceramics by flash sintering. *Ceram Int* 2022, **48**: 16455–16460.
[46] Aoki Y, Masuda H, Yoshida H. Formation of Al_2O_3–$GdAlO_3$ eutectic ceramics with a fine anisotropic structure in a flash event. *J Am Ceram Soc* 2023, **106**: 3336–3342.
[47] Yao S, Liu YS, Liu DG, *et al.* Effect of the Al_2O_3 content on the microstructure evolution of flash-sintered Al_2O_3–8YSZ ceramics. *Open Ceram* 2023, **16**: 100468.
[48] Liu GX, Liu DG, Liu JL, *et al.* Asymmetric temperature distribution during steady stage of flash sintering dense zirconia. *J Eur Ceram Soc* 2018, **38**: 2893–2896.
[49] Xu X, Fan JY, Liu JL, *et al.* Formation of eutectic structure in dense Al_2O_3–YAG composite by electric field treatment. *Ceram Int* 2021, **47**: 23647–23652.
[50] Liu HF, Su HJ, Shen ZL, *et al.* Formation mechanism and roles of oxygen vacancies in melt-grown Al_2O_3/$GdAlO_3$/ZrO_2 eutectic ceramic by laser 3D printing. *J Adv Ceram* 2022, **11**: 1751–1763.
[51] Raj R. Joule heating during flash-sintering. *J Eur Ceram Soc* 2012, **32**: 2293–2301.
[52] Jones GM, Biesuz M, Ji W, *et al.* Promoting microstructural homogeneity during flash sintering of ceramics through thermal management. *MRS Bull* 2021, **46**: 59–66.
[53] Chaim R. Reactive flash sintering (RFS) in oxide systems: Kinetics and thermodynamics. *J Mater Sci* 2021, **56**: 278–289.
[54] LLorca J, Orera VM. Directionally solidified eutectic ceramic oxides. *Prog Mater Sci* 2006, **51**: 711–809.
[55] Kok D, Yadav D, Sortino E, *et al.* α-Alumina and spinel react into single-phase high-alumina spinel in < 3 seconds during flash sintering. *J Am Ceram Soc* 2019, **102**: 644–653.
[56] Shen C, Niu T, Yang B, *et al.* Micromechanical properties and microstructures of AC and DC flash-sintered alumina. *Mat Sci Eng A—Struct* 2023, **866**: 144631.
[57] Liu JL, Chen LY, Liu GX, *et al.* The onset mechanism of flash sintering dense 8YSZ. *Mater Solidif* 2025, **1**: 9580011.
[58] Su XH, Li WJ, Chen D, *et al.* Rapid fabrication of oxygen-deficient zirconia by flash sintering treatment. *J Adv Ceram* 2024, **13**: 1881–1890.
[59] Yang YJ, Motley NB, Mecartney ML, *et al.* Mechanical properties of Al_2O_3–$LaPO_4$ composites with eutectic microstructure produced by flash sintering. *J Am Ceram Soc* 2024, **107**: 3028–3044.
[60] Pastor JY, LLorca J, Salazar A, *et al.* Mechanical properties of melt-grown alumina–yttrium aluminum garnet eutectics up to 1900 K. *J Am Ceram Soc* 2005, **88**: 1488–1495.
[61] Nie Y, Zhang MF, Liu Y, *et al.* Microstructure and mechanical properties of Al_2O_3/YAG eutectic ceramic grown by horizontal directional solidification method. *J Alloy Compd* 2016, **657**: 184–191.
[62] Su HJ, Zhang J, Cui CJ, *et al.* Rapid solidification behaviour of Al_2O_3/$Y_3Al_5O_{12}$ (YAG) binary eutectic ceramic *in situ* composites. *Mat Sci Eng A—Struct* 2008, **479**: 380–388.
[63] Zhao D, Su HJ, Liu HF, *et al.* Densification and microstructural evolution of bulk Al_2O_3–$Y_3Al_5O_{12}$ (YAG) eutectic ceramic fabricated by spark plasma sintering. *Ceram Int* 2019, **45**: 12337–12343.
[64] Wang X, Tian ZL, Zhang W, *et al.* Mechanical properties of directionally solidified Al_2O_3/$Y_3Al_5O_{12}$ eutectic ceramic prepared by optical floating zone technique. *J Eur Ceram Soc* 2018, **38**: 3610–3617.